Dalton Transactions

ROYAL SOCIETY OF CHEMISTRY

PAPER

View Article Online
View Journal | View Issue

Published on 31 October 2024. Downloaded by Argonne Research Library on 12/20/2024 5:09:57 PM.

Check for updates

Cite this: *Dalton Trans.*, 2024, **53**, 19246

The effect of second coordination sphere interactions on the magnetic anisotropy of transition metals†

Sofie S. Leiszner, [a] Mauro Perfetti, [b] Emil Damgaard-Møller,[a] Yu-Sheng Chen[c] and Bo B. Iversen *[a]

In the study of mononuclear transition metal single molecule magnets (SMMs), extensive research has concentrated on identifying optimal coordination geometries around the central metal ion to enhance SMM properties. However, the role of non-covalent interactions in the second coordination sphere has been relatively underexplored. Here, we study the impact of non-covalent Cl···H interactions on the magnetic anisotropy of the central Co(II) ion in the distorted axially compressed octahedral complex $CoCl_2(tu)_4$ (**1**) (tu = S=C(NH$_2$)$_2$). By performing cantilever torque magnetometry on **1**, the orientation of the magnetic easy axis is found to deviate by almost 40° from the axial Co–Cl bond. Theoretical modelling on structural modifications of the structure of **1**, quantifies how the distance between the Cl ligand and the nearest H-atom significantly influences the orientation of the magnetic easy axis and the *D*-value. Experimental chemical bonding analysis based on multipole modelling of synchrotron X-ray diffraction data on **1** reveal that the nearby H-atoms polarize the electron density of the Cl-ligands. This polarization results in reduced electron density at the axial positions on the Co octahedra, explaining the calculated increase in the magnitude of the *D*-value, when the H-atoms are moved away from Cl *in silico*. Topological analysis of theoretical electron densities on modified structures of **1** corroborates an increase in the electron density at the Co–Cl bond critical point, as the nearby H-atoms are moved further from Cl. These findings demonstrate the significant influence that non-covalent interactions have on the magnetic anisotropy of mononuclear transition metals and opens the possibility of utilizing these interactions in the design of transition metal based SMMs.

Received 14th October 2024,
Accepted 30th October 2024

DOI: 10.1039/d4dt02873b

rsc.li/dalton

Introduction

Single molecule magnets (SMMs) have applications in many fields such as quantum computing,[1–3] high-density information storage[4] and molecular spintronics.[5] The primary objective within the field is obtaining stable magnetic states at room temperature,[6] by engineering a high anisotropy barrier, which can give a high blocking temperature. These features are strictly dependent on the magnetic anisotropy of the metal ion, *i.e.* the directional dependence of its' magnetic properties. The interplay between structure and magnetic anisotropy is fundamental in the quest to design robust SMMs. This pursuit often entails selecting a favourable coordination geometry around the central metal ion or modifying the ligand field strength.[7–14]

Lanthanides, known for their large first order angular momentum, have traditionally dominated SMM research.[6,15–19] The magnetic anisotropy of lanthanide ions can be maximized by matching the ligand field to the intrinsic electron distribution (either oblate or prolate) of the given lanthanide ion. This approach lead to a groundbreaking 2018 study, where a dysprosium SMM was shown to exhibit magnetic hysteresis above liquid-nitrogen temperatures.[20]

In the case of transition metal SMMs, most research has similarly focused on identifying favourable coordination geometries in the first coordination sphere that would lead to strong axial magnetic anisotropy, characterized by a large negative *D*-value and a comparably small *E*-value.[11,21–23] In this regard, Co(II) based complexes are of particular interest due to their Kramers' nature, featuring a bistable spin ground state that effectively suppresses quantum tunnelling of the

[a]*Center for Integrated Materials Research, Department of Chemistry and iNANO, Aarhus University, Langelandsgade 140, DK-8000 Aarhus C, Denmark. E-mail: bo@chem.au.dk*
[b]*Department of Chemistry "U. Schiff", University of Florence, via della Lastruccia 3-13, 50019 Sesto Fiorentino, Italy*
[c]*ChemMatCARS, The University of Chicago, Lemont, IL 60439, USA*
† Electronic supplementary information (ESI) available. See DOI: https://doi.org/10.1039/d4dt02873b

This journal is © The Royal Society of Chemistry 2024

Published on 31 October 2024. Downloaded by Argonne Research Library on 12/20/2024 5:09:57 PM.

magnetization.[12,24,25] A prominent example is the linear complex $Co(C(SiMe_2ONaph)_3)_2$, which has a sufficiently weak ligand field, allowing it to adopt a non-Aufbau ground state of maximum orbital angular momentum and a strong, unquenched spin orbit coupling.[26]

However, while first coordination sphere interactions have received significant attention, other factors such as second coordination sphere interactions have often been overlooked.[27] Some recent studies of $[Ln(NO_3)_3(H_2O)_3]\cdot$(18-crown-6) complexes have shown how the encapsulation of the complex in the crown ether has detrimental effects on the SMM properties of the compounds by reducing the anisotropy barrier and changing the orientation of the magnetic easy axis.[28,29] Similar effects have been seen for other lanthanide compounds, where removal or weakening of the second coordination sphere interactions has led to improved SMM properties.[30,31] These studies highlight the broader potential of second coordination interactions in enhancing the energy barriers and blocking temperatures of SMMs. However, their influence in transition metal SMMs remains relatively unexplored, despite the more easily controllable coordination environment in these systems, which should allow for finer tuning of the magneto-structural correlations. Furthermore, many techniques employed in the study of SMMs yield signals from the entire crystal lattice, not a single molecule. A crystal may encompass many strong second coordination sphere interactions, potentially influencing the magnetic anisotropy of the central metal ion.

In this study, we explore the interplay between second coordination sphere interactions and magnetic anisotropy in $CoCl_2(Tu)_4$ (**1**), where Tu = thiourea ($S{=}C(NH_2)_2$). The Co(II) complex assumes a distorted axially compressed octahedral geometry, featuring two shorter Co–Cl bonds in the axial positions and four longer Co–S bonds in the plane (Fig. 1). The axial compression causes a destabilization of the orbitals having a *z*-component (*i.e.* d_{xz}, d_{yz} and d_{z^2}), which lifts the degeneracy of the e_g and t_{2g} orbital pairs (Fig. 2). This leads to an almost degenerate d_{xz} and d_{yz} orbital pair that collectively accommodate three electrons, which is highly desirable for achieving a strong magnetic anisotropy in a Co(II) complex.[32]

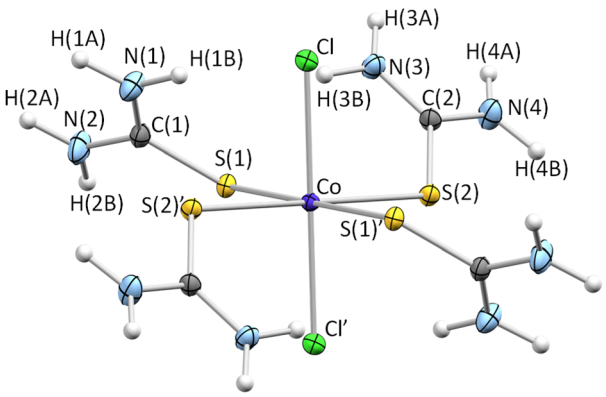

Fig. 1 Single crystal X-ray diffraction structure of **1** shown with 90% probability ellipsoids. Co is on a special position of inversion symmetry. The atoms from the other asymmetric unit are marked with an apostrophe ('). Atom colors: Co (dark blue), Cl (green), S (yellow), C (grey), N (light blue), H (white).

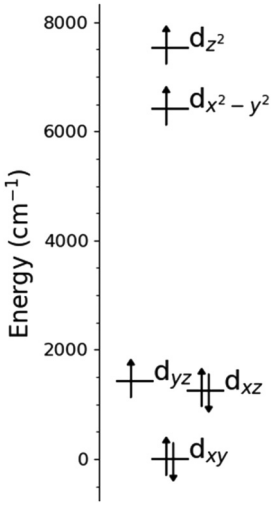

Fig. 2 AILFT orbital splitting for $\mathbf{1}^{ND}$. The lobes of the d_{z^2} orbital are along the Co–Cl bond, while the lobes of the $d_{x^2-y^2}$ orbitals are along the Co–S bonds. Obtained from a CASSCF-NEVPT2 calculation in ORCA following the procedure described in the Experimental section.[35]

The relation between the structure and magnetic anisotropy of **1** was explored by Tripathi *et al.* in 2021,[33] and the magnetic susceptibility tensor, χ, was experimentally measured using single-crystal polarized neutron diffraction (SC-PND). The largest eigenvalue of the χ-tensor is more than twice as large as the intermediate value, demonstrating the axiality of the system. Using the eigenvectors of this tensor, they found that the easy axis of magnetization was tilted with respect to the Co–Cl bond. A similar tilt of the easy axis with respect to the Co–ligand bonds has also been observed in another octahedral Co(II) compound using SC-PND.[34] These observed tilts of the easy axes are unexpected, given the conventional understanding linking ligand field and magnetic anisotropy, which would predict the easy axis along the Co–Cl bond. Hence, it is plausible that certain effects in the ligand field that has previously been overlooked, might contribute to the tilted easy axes.

Here, we unravel the reason behind the tilted easy axis of these systems, using compound **1** as our model system. Initially, we employ cantilever torque magnetometry (CTM) to experimentally detect the orientation of the magnetic axes of **1**. Secondly, we construct a multipole model (MM) of the electron density to investigate how the inter- and intramolecular Cl–H interactions affect the electron density distribution around the Co(II) center in **1**. Lastly, a series of theoretical *ab initio* calculations on modified structures of **1** reveal the strong correlation between the orientation of the easy axis and *D*-value with the Cl–H distance. By bridging advanced experimental and theoretical tools, we provide a rationale for the observed tilt of the easy axis in **1** and suggest new potential

Published on 31 October 2024. Downloaded by Argonne Research Library on 12/20/2024 5:09:57 PM.

routes for synthesizing novel transition metal SMMs with enhanced magnetic anisotropy by clever design of the second coordination sphere non-covalent interactions.

Experimental section

Synthesis of $[CoCl_2(tu)_4]$ (tu = thiourea (S═C$(NH_2)_2$)) (1)

The crystals of $[CoCl_2(tu)_4]$ (**1**) where tu = thiourea (S═C$(NH_2)_2$) were synthesized by reacting cobalt chloride hexahydrate with thiourea in alcoholic solution by a previously published procedure.[33]

Single crystal synchrotron X-ray diffraction

Single crystal X-ray diffraction data were collected on a Huber Chi 3-circle diffractometer equipped with a Dectris Pilatus3X-1M CdTe detector at the Advanced Photon Source beamline 15ID-D operated by ChemMatCARS of the Argonne National Lab. The data were collected with an energy of 40 keV (0.30996 Å) and at a temperature of 20(1) K using an open-flow Oxford Helijet cryostat. The Pilatus frames were converted to the Bruker .sfrm format and appropriate integration masks were generated using a local program (Pilatus-fc).[36] The frames were reduced using SAINT,[37] and the raw data were further processed, scaled and corrected for absorption using SADABS.[38] The data was subsequently merged using the robust/resistant Tukey weighting as implemented in SORTAV,[39] and the structure was solved using SHELXT[38] and refined by full-matrix least-squares against F^2 using SHELXL-2014/7 [38] within the SHELXle graphical user interface.[40] This model was then used as the starting point for the electron density investigation in XD2016.[41] See Table S1† for additional crystallographic information.

Electron density analysis

The electron density was modelled by the Hansen–Coppens multipole density formalism.[42] The multipole model (MM) partitions the electron density of a given atom, $\rho_{atom}(\boldsymbol{r})$, into three components each corresponding to a term in eqn (1): a spherical core density, a spherical valence density and an aspherical valence density.

$$\rho_{atom}(\boldsymbol{r}) = P_c\rho_c(\boldsymbol{r}) + P_v\kappa^3\rho_v(\kappa\boldsymbol{r}) + \sum_{l=0}^{l_{max}}\kappa'^3 R_l(\kappa' r)\sum_{m=0}^{l} P_{lm\pm}d_{lm\pm}(\theta,\varphi) \quad (1)$$

Here P_c, P_v, and $P_{lm\pm}$ are the multipole population parameters for the core, spherical valence, and aspherical valence density, respectively. κ and κ' are the expansion/contraction-parameters for the spherical and aspherical part of the valence electron density. The radial functions, $R_l(\kappa'\boldsymbol{r})$, are nodeless single-zeta Slater functions with optimized coefficients and exponents. The functions denoted $d_{lm\pm}$ are angular functions that resembles hydrogen-like orbitals.[43]

Since Co(II) in **1** lies on a special position of inversion symmetry, only multipole populations of even order spherical harmonic functions are refined for Co. Additionally, pseudo-symmetry constraints were applied to reduce the number of refinable parameters (see Table S2† for applied symmetries). The local coordinate system of Co was chosen to have the *z*-axis towards Cl and the *y*-axis towards S(1). The N–H distances were constrained to 1.013 Å as obtained from tabulated neutron diffraction (ND) data.[44] In addition, the magnitude of the H-atoms isotropic atomic displacement parameters (ADPs) were set to depend on the ADPs of the N-atom to which they are bonded. All H-atoms were constrained to have the same multipole population parameters. The expansion/contraction parameters, κ and κ', were refined for all non-H-atoms, except κ' for Co which was set to 1.0 as the refinement of this parameter was unstable. The values for the H-atoms were set to 1.1 and 1.13 for κ and κ', respectively.[45] Anisotropic ADPs were refined for all non H-atoms, and the anharmonic model using the Gram–Charlier expansion up to the third order was introduced for Cl. The total integrated negative nuclear probability density for Cl was negligible. The final model had an $R(F)$-factor of 1.54% (compared with 1.81% for the independent atom model refined in SHELXT). The final MM had a parabolically shaped fractal dimension plot (Fig. S1†) with maximum and minimum residuals of 0.32 e Å^{-3} and −0.34 e Å^{-3}.

Computational details

All quantum-chemical calculations were performed using the ORCA 4.1 software[35] on the previously published crystal structure from neutron diffraction (ND)[33] referred to as $\mathbf{1}^{ND}$ as well as several modifications of this structure. Multi-reference *ab initio* calculations were used to calculate the *D*-value, *E*-value, and the *g*-matrix. State-average complete-active-space self consistent-field (CASSCF) calculations were performed, and dynamic correlations included using N-electron valence perturbation theory to the second order (NEVPT2). The Ahlrichs polarized triple-ζ (def2-TZVP) quality basis set was used for all atoms. A scalar relativistic correction was applied using the Douglas–Kroll–Hess approach[46,47] and the spin–orbit coupling was treated using the mean-field (SOMF) approximation.[48–51] The calculations were performed with an active space of CAS(7,5), which corresponds to seven active d electrons in five active d-orbitals and computed 10 quartets as well as 40 doublets in the configuration interaction (CI) procedure to extract the desired parameters.

Cantilever torque magnetometry

Cantilever torque magnetometry (CTM) measurements were performed on a single crystal of **1** for three different orientations of the crystal (see Table S5†). The face indexed crystal is placed on a cantilever and rotated by an angle θ around a given rotation axis perpendicular to the applied magnetic field. The CTM technique employed here uses capacitive detection of the deflection of the upper plate (the cantilever). The measured capacitance is proportional to the magnetic torque, $\boldsymbol{\tau}$, which is in turn related to the magnetization of the sample, $\boldsymbol{M}$, in an applied magnetic field, $\boldsymbol{B}$, by the following vector product:

$$\boldsymbol{\tau} = \boldsymbol{M} \times \boldsymbol{B} \quad (2)$$

This journal is © The Royal Society of Chemistry 2024

Published on 31 October 2024. Downloaded by Argonne Research Library on 12/20/2024 5:09:57 PM.

Therefore, measurements of the magnetic torque at different orientations of the crystal gives insights into the angular dependence of its magnetic properties, making CTM an ideal technique for detecting the orientation of the principal magnetic axes.[52]

All measurements were performed at 2.0 K and various strengths of the static magnetic field up to 12 T. Subsequent data treatment was performed using a home-written program in MATLAB[53] based on the package EasySpin.[54]

Results and discussion

Crystal structure

Compound **1** crystallizes in the tetragonal space group $P4_2/n$ (see Table S1† for crystallographic information) with the Co(II) ion located on a special position of inversion symmetry. The crystal structure of **1** is shown in Fig. 1 and relevant bond distances and angles are given in Table 1. The Co–Cl bond lengths of 2.4657(1) Å are shorter than the two Co–S bonds of 2.50638(4) Å and 2.54953(4) Å, validating that **1** is axially compressed. However, the two Co–S bond lengths are also significantly different from one another, and the L–Co–L angles cover the range from 84.5° to 95.5°, demonstrating some structural deviation from the D_{4h} symmetry in the first coordination sphere (see Table S3† for Co to ligand bond lengths and angles, and for comparison to ND results[33]).

Table 1 Selected distances and bond angles in **1**. Atoms marked with an apostrophe (′) are from the other asymmetric unit. Atoms marked with a star (*) are from another molecule of **1** in the crystal structure (intermolecular interactions)

Distances (Å)		Bond angles (°)	
Co–Cl	2.4657(1)	S(1)–Co–Cl	92.270(2)
Co–S(1)	2.50638(4)	S(2)–Co–Cl	95.481(3)
Co–S(2)	2.54953(4)	S(1)′–Co–Cl	87.730(2)
Cl–H(1B)	2.2782(1)	S(2)′–Co–Cl	84.519(3)
Cl–H(3B)	2.71905(9)	S(1)–Co–S(2)	87.725(1)
Cl–H(1A)*	2.56704(9)	S(1)–Co–S(2)′	92.28(1)
Cl–H(2A)*	2.3269(1)		
Cl–H(3A)*	2.7832(1)		
Cl–H(4A)*	2.3769(1)		

The unit cell contains four molecules of **1**, and the shortest Co–Co distance in the structure is 8.092 Å. As seen from Table 1, the crystal structure also contains six short Cl–H distances; two intramolecular and four intermolecular ranging from 2.28 to 2.72 Å (see Table S4† for comparison to ND values[33]). All these distances are shorter than the sum of the van der Waals radii of Cl and H, with the shortest being the intramolecular Cl–H(1B) distance of 2.2782(1) Å. The H-atoms are positioned perpendicular to the Co–Cl bond, thereby residing on the nucleophilic site of the Cl atom (Fig. S2†). Furthermore, the shortest of the Cl–H interactions is in the direction of the tilt of the easy axis which leads us to suspect that these short Cl–H interactions might influence the magnetic anisotropy of Co.

Experimental measure of magnetic anisotropy

To gain insights into the angular dependence of the magnetic anisotropy of Co, CTM measurements have been performed on a single crystal of **1**. Since the measured torque arises from all magnetic centers in the crystal, all non-collinear molecules in the unit cell must be considered. In the case of **1**, there are four non-collinear molecules in the unit cell, which are related by the four-fold rotation of the space group.

The magnetic torque was measured for three different orientations of the crystal (Table S5†). For each orientation, the crystal was rotated around a rotation axis for several different field strengths at a temperature of 2.0 K. The measured data is displayed in Fig. 3. Since all measurements were performed at 2.0 K, we assume that only the lowest Kramers' doublet is thermally populated, which allows us to treat the system as an effective spin $S' = \frac{1}{2}$ system. Therefore, the Zeeman splitting, describing the splitting of the m_s states in an applied magnetic field, is the only term included in the Hamiltonian given in eqn (3):

$$\hat{H} = \hat{H}_{\text{Zeeman}} = \mu_B \boldsymbol{B} \tilde{g}' \hat{\boldsymbol{S}}' \quad (3)$$

where $\boldsymbol{B}$ is the magnetic field vector, $\tilde{g}'$ is the effective spin $\frac{1}{2}$ g-tensor and $\hat{\boldsymbol{S}}'$ is the effective electron spin operator.

The overall shape of the model and the zero-torque points fit the data well, which implies that the orientation of the magnetic axes is accurate. The final model gave rise to the mag-

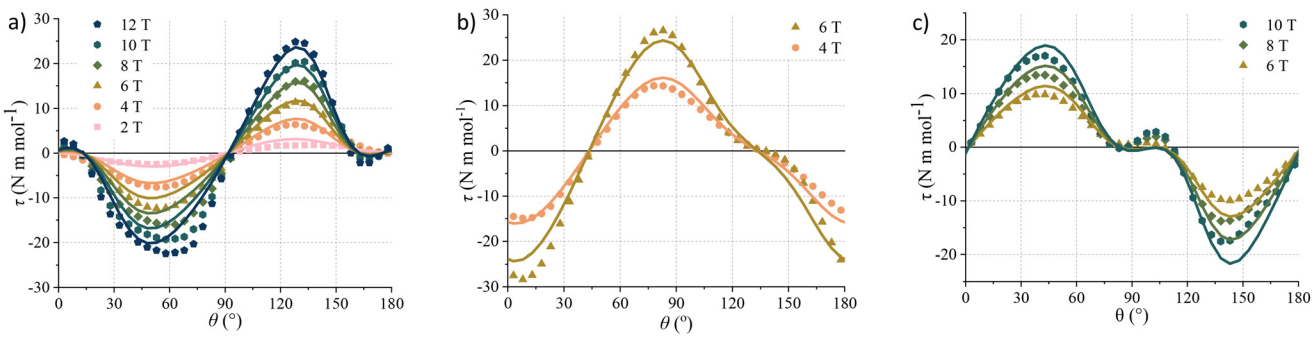

Fig. 3 (a–c) The magnetic torque, τ, measured by CTM plotted as a function of the rotation angle, θ, for the three different orientations of the crystal of **1** and several different magnetic field strengths (given in the legend). All data have been collected at a temperature of 2.0 K.

Published on 31 October 2024. Downloaded by Argonne Research Library on 12/20/2024 5:09:57 PM.

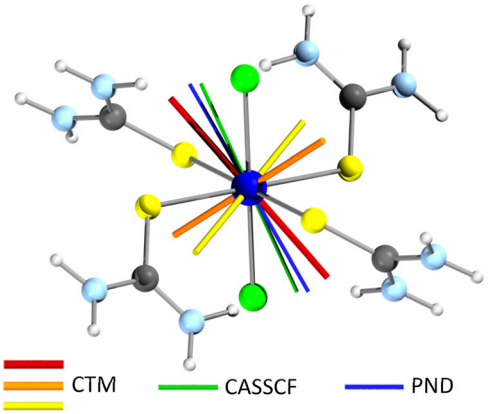

Fig. 4 The orientation of the magnetic axes of Co(II) in **1** from the CTM fit: easy axis (red), intermediate axis (orange) and hard axis (yellow). The easy axes from CASSCF (green) and PND[33] (blue) are shown for comparison. The angle between the CTM and the PND easy axes is 11.5°, the one between CTM and CASSCF is 18.4° and the one between CASSCF and PND is 12.2°. Atom colors: Co (dark blue), Cl (green), S (yellow), C (grey), N (light blue), H (white).

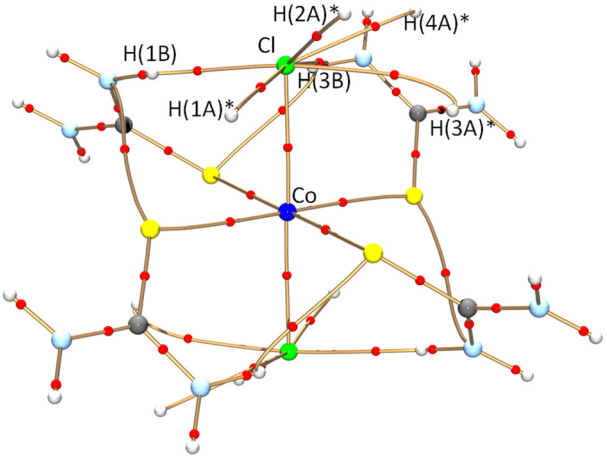

Fig. 5 Molecular graph for **1**, including the four H-atoms from other molecules that interact with Cl. BCPs are marked with red spheres and bond paths with golden cylinders. H-atoms from other molecules in the crystal are marked with a star (*). An enlarged version of this figure and a view of the molecular graph along the Co–Cl bond are included in Fig. S3.† Atom colors: Co (dark blue), Cl (green), S (yellow), C (grey), N (light blue), H (white).

netic axes shown on Fig. 4 and a fairly rhombic effective $\tilde{g}'$ matrix with g_1 = 2.67, g_2 = 3.79, g_3 = 6.95 (see Table S6† for tabulated fit result). The orientation of the magnetic axes are given in Table S7† and the orientation of the easy axis is compared to PND[33] and CASSCF in Tables S8 and S9.† The found easy axis deviates by almost 40° from the Co–Cl bond, and fits well with the ones found by PND[33] and CASSCF, showing deviations between the three determined easy axes of less than 20° (Table S9†).

Critical points in the electron density

Critical points in the electron density identify interactions between atoms in molecules and are points where the derivative of the electron density, $\nabla\rho(\boldsymbol{r})$, is zero. For this study, the most relevant type of critical points is the bond critical point (BCP), which is a point in real space where the electron density increases towards the point in two directions (perpendicular to the bond) and decreases towards the point in one direction (along the bond).

To investigate the interactions between Cl and the six surrounding H-atoms (Fig. S2†), the MM electron density of **1** has been searched for BCPs (Fig. 5), and BCPs are found between Cl and all six neighbouring H-atoms. In contrast, no BCPs were observed between Co and the H-atoms, suggesting that the H-atoms predominantly interact with Cl, not Co.

For the Cl–H BCPs shown in Fig. 5, the electron density at the BCP, ρ_{BCP}, is small, and the energy is dominated by the kinetic energy, G_b (Table S10†) and the Laplacian of the electron density at the BCP is positive (Table S11†). This shows that the Cl–H interactions are closed shell interactions as expected for these hydrogen-like-bonds. Expectedly, a comparison of the topological properties of the BCPs reveals no significant difference between the intra- and intermolecular Cl–H interactions (Tables S6 and S7†). However, splitting the H-atoms in two groups based on their Cl–H distance reveal clear trends: the interactions with the shorter Cl–H bonds (marked in bold in Tables S10 and S11†) show larger ρ_{BCP}, $\nabla^2\rho_{BCP}$ and λ_3, which indicates stronger interactions.

The static deformation density and the Laplacian

To investigate the various interactions of the H-atoms with Cl, the static deformation density and the Laplacian are employed. The static deformation density, $\Delta\rho(\boldsymbol{r})$, is the difference between the electron density from the MM, $\rho_{MM}(\boldsymbol{r})$, and the electron density from the independent atom model (IAM), $\rho_{IAM}(\boldsymbol{r})$:

$$\Delta\rho(\boldsymbol{r}) = \rho_{MM}(\boldsymbol{r}) - \rho_{IAM}(\boldsymbol{r}) \quad (4)$$

The deformation density highlights the aspherical features of the electron density such as bonding and lone-pair regions.[55] The Laplacian, $\nabla^2\rho(\boldsymbol{r})$, is the trace of the second order derivative of the electron density. The sign of the Laplacian indicates local electronic charge concentrations ($\nabla^2\rho(\boldsymbol{r}) < 0$) and local charge depletion ($\nabla^2\rho(\boldsymbol{r}) > 0$) with respect to the immediate surroundings.

The static deformation density and the negative Laplacian have been calculated in the six Co–Cl–H(L) planes with L = 1A, 1B, 2A, 3A, 3B and 4A. The plots for H(1B) are given in Fig. 6, and the remaining plots are shown in Fig. S4.† Critical points in the negative Laplacian are shown in Fig. S5.† The electron density on Cl is aspherical with excess electron density pointing towards the nearby H-atoms (elongated blue contours lines on Cl towards H(1B) in Fig. 6a), whereas electron depletions on H(1B) (red lobes) point towards Cl in Fig. 6a. As seen on Fig. 6b, Cl has a maximum in the negative Laplacian pointing towards H(1B), demonstrating the strength of this interaction, which was also apparent from the relatively large ρ_{BCP} in the Cl–H(1B) BCP (Table S11†).

This journal is © The Royal Society of Chemistry 2024

Published on 31 October 2024. Downloaded by Argonne Research Library on 12/20/2024 5:09:57 PM.

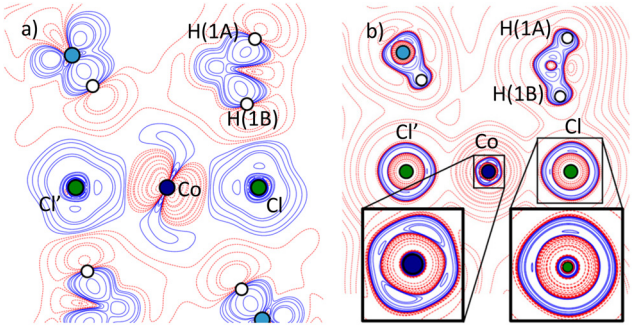

Fig. 6 2D plot of the static deformation density (a) and the negative Laplacian, $-\nabla^2\rho(\boldsymbol{r})$ (b) in the Co–Cl–H(1B) plane. Dashed red lines indicate negative contours and solid blue lines indicate positive contours. The contour lines for the static deformation density are drawn from −2.0 e Å^{-3} to 2.0 e Å^{-3} in steps of 0.05 e Å^{-3}. Negative Laplacian contour lines are drawn at: $a \times 10^n$ e Å^{-5}, with a = 1, 2, 4, 8 and n = −2, −1, 0, 1, 2, 3, 4.

Quantifying the effect of the intramolecular Cl–H interactions by theoretical calculations

CASSCF-NEVPT2 calculations have been performed within the software package ORCA 4.1 [35] on the structure of $\mathbf{1}^{ND}$ to give the *ab initio* ligand field theory (AILFT) orbital splitting given in Fig. 2. In the CASSCF calculations, we employ the spin quantum number S to describe the states of the Co(II) ion instead of the total angular momentum quantum number J, despite its unquenched orbital angular momentum (OAM) of $L \approx 1$ (Fig. 2). This has proven to be a reasonable approach for several reasons. First, the spin orbit coupling is accounted for using the mean-field SOMF approximation.[50,51] Secondly, the impact of the OAM is modest, since L is not maximized ($L \neq 3$) as was the case for the linear non-Aufbau Co(II) complex reported by some of us in 2018.[26] Lastly, as will be elaborated in the forthcoming paragraph, the results from the CASSCF calculation on the structure of $\mathbf{1}^{ND}$ are in excellent agreement with the employed experimental methods.

The CASSCF-NEVPT2 calculation on the structure of $\mathbf{1}^{ND}$ yielded a negative D-value of −81.1 cm^{-1} and a strong rhombic term E of 18.5 cm^{-1}. These values are consistent with the χ-tensor found by PND,[33] where one eigenvalue of the χ-tensor is significantly larger than the remaining two in line with the large negative D-value found by these calculations, while the large difference between the two smaller eigenvalues of the χ-tensor explains the large rhombic term from the calculation. The obtained g_{zz}^{calc} vector from the CASSCF-NEVPT2 calculation on $\mathbf{1}^{ND}$, corresponding to the easy axis, is found to be tilted by 21.5° with respect to the Co–Cl bond. The orientation of the easy axis reproduces those determined by the experimental methods (CTM and PND), thereby enhancing our confidence in the CASSCF calculations (see Fig. 4 and section 2 of the ESI†). The excellent agreement between the experimental electron density and the electron density from the CASSCF wavefunction further justifies the reliability of the theoretical results (see section 4a in the ESI†).

As explained previously, the first coordination sphere around Co(II) in **1** does not strictly conform to the D_{4h} symmetry, due to unequal Co–S bond lengths and L–Co–L angles that differ from 90° (Table 1). To investigate the impact of the distortions from D_{4h} in the first coordination sphere, we modify *in silico* the structure of $\mathbf{1}^{ND}$ such that the two Co–S bonds are set to the average Co–S bond length of 2.5245 Å by translating the thiourea ligands along their respective Co–S bonds. The resulting CASSCF calculation on the modified structure showed only a slight increase in the absolute magnitude of D and no significant change in the angle between the easy axis and the Co–Cl bond (Table S13†).

Additionally, forcing all S–Co–S angles to be exactly 90°, gave an increase in the absolute magnitude of D of 13.7 cm^{-1} and reduced the angle between the easy axis and the Co–Cl bond by 1.4°. Additionally, tilting the Cl–Co–Cl axis with respect to the CoS_4 plane such that all Cl–Co–S angles are also exactly 90°, corresponding to exact D_{4h} symmetry in the first coordination sphere referred to as the $\mathbf{1}_{D_{4h}}^{ND}$ structure, increased the D-value to −105.4 cm^{-1}. The angle between the easy axis and the Co–Cl bond remained around 23°, but the orientation of the easy axis changed, such that its projection in the CoS_4 plane is closer to S(1) than S(2)′ (Fig. S8†). This shows that the D-value is significantly affected by the deviations from D_{4h} symmetry in the first coordination sphere, while the easy axis tilt angle is more or less unchanged, although its orientation changes in the case of D_{4h} symmetry in the first coordination sphere.

Since the distortions from D_{4h} in the first coordination sphere cannot explain the tilt of the easy axis, we suspect that interactions along Co–Cl could have an impact on the tilt angle. The earlier investigations of the experimental charge density showed significant interactions between Cl and the nearby H-atoms. To investigate the impact of these short Cl–H interactions on the magnetic anisotropy, a series of CASSCF calculations have been performed on *in silico* permutations of the structure $\mathbf{1}^{ND}$. Rotations in small increments have been performed around the C(1)–N(1) bond and the symmetry related C(1)′–N(1)′ bond, corresponding to rotations around the red axes in Fig. 7. A CASSCF calculation has been performed on each permutated structure, for which the obtained easy axes are plotted in Fig. 7 (see Fig. S9† for view along the Co–Cl bond). From this plot, the strong correlation between the minimum Cl–H distance and the orientation of the magnetic easy axis is clear; increasing the Cl–H distance, moves the easy axis closer to the Co–Cl bond.

In Fig. 8, the angle between the easy axis and the Co–Cl bond (left vertical axis) and the calculated D-value (right vertical axis) are plotted *versus* the Cl and H(1B) distance in each of the structures. Similar to Fig. 7, this plot also shows that increasing the Cl–H distance, rotates the easy axis towards the Co–Cl bond by decreasing the angle from 21.5° to 14.9°. In addition, it causes a significant increase in the magnitude of D from −81.1 cm^{-1} to −93.0 cm^{-1}.

As found earlier, in addition to the Cl–H(1B) interaction, there is also a short Cl–H(3B) interaction. As H(1B) is rotated

Published on 31 October 2024. Downloaded by Argonne Research Library on 12/20/2024 5:09:57 PM.

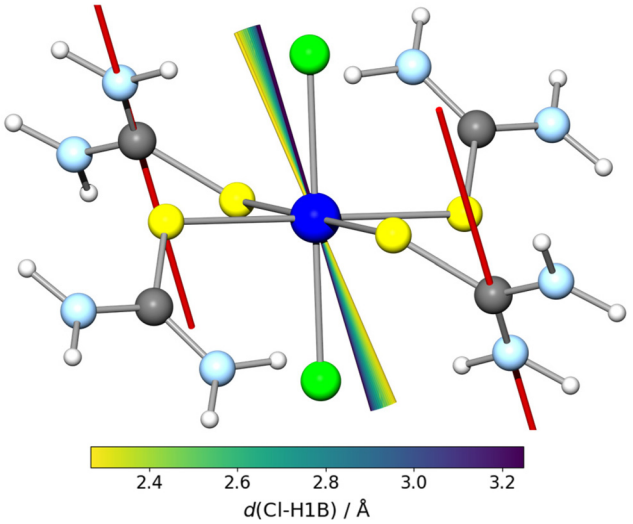

Fig. 7 The $\mathbf{1}^{ND}$ structure with the calculated easy axes for the rotations along the C(1)–N(1) axis shown in red. A color gradient is added to visualize the easy axes' dependence on the Cl–H(1B) distance. Atom colors: Co (dark blue), Cl (green), S (yellow), C (grey), N (light blue), H (light grey).

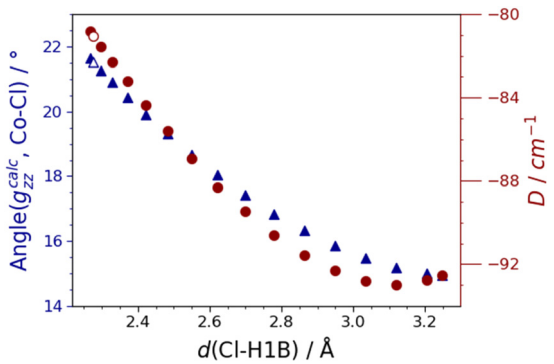

Fig. 8 The angle between the CASSCF easy axis and the Co–Cl bond (blue triangles) and the *D*-value (red circles) plotted as a function of the Cl–H(1B) distance for the *in silico* rotations around C(1)–N(1) bond (and the symmetry related C(1)′–N(1)′ bond) in the $\mathbf{1}^{ND}$ structure. The results from the CASSCF calculation on the non-modified $\mathbf{1}^{ND}$ structure are shown as open symbols.

away from Cl, H(3B) quickly becomes the H-atom closest to Cl. After rotating H(1B) as far away as possible, we performed *in silico* rotations around the C(2)–N(3) axis (and the symmetry related C(2)′–N(3)′ axis) on the same structure. As seen from Fig. 9, this leads to even further increases in the magnitude of *D* to −108.0 cm^{-1} and a further decrease in the tilt of the easy axis to 13.4°. Similar rotations have been performed on the structure with D_{4h} symmetry in the first coordination sphere reaching a *D*-value of −129.9 cm^{-1} and a tilt of the easy axis of 13.3°. This once again highlights the independence of the tilted easy axis on the deviations in the first coordination sphere. It should be noted that these rotations around C–N bonds rotates the H-atoms out of the plane of the thiourea

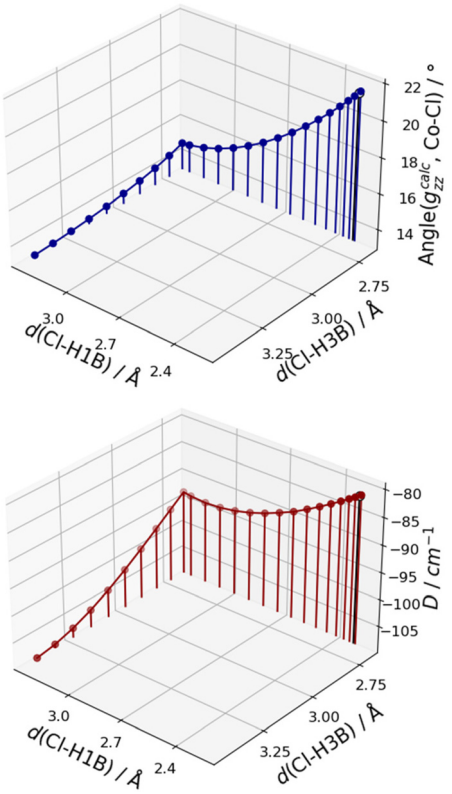

Fig. 9 The angle between the easy axis and the Co–Cl bond (top) and the *D*-value (bottom) plotted as a function of the Cl–H(1B) and Cl–H (3B) distance in the modified structures of $\mathbf{1}^{ND}$. The results from the non-modified $\mathbf{1}^{ND}$ structure are shown as open circles in black.

ligand. If instead, rotations are performed along all the S=C axes (Fig. S17†), thiourea is kept planar. We have also performed calculations with rotations along the S=C axes, which ultimately showed a similar dependence between the Cl–H distance and the tilt of the easy axis and the *D*-value (Fig. S18 and S19†). We note that this rotation also has an impact on the Co–S interaction, as it rotates the coordinating lone pair on S away from Co.

Overall, these findings suggest that the Cl–H interactions have a strong effect on the magnetic anisotropy of Co in **1**. In addition, it highlights the potential importance of all six Cl–H interactions in the crystal structure.

As shown in the section on the static deformation density and the Laplacian, the interaction between H and Cl leads to a polarization of Cl, causing a shift of electron density from Cl towards the nearby H. To understand how this interaction affects the electron density around Co, a topological analysis of the calculated wavefunction for each structure has been performed in the software package AIMAll.[56]

These results show that as H(1B) is moved further from Cl using the C–N rotations, the electron density on Cl and the electron density in the Co–Cl BCP increases (Fig. S10 and S11†). This results in more electron density along the axial positions of the Co octahedra, which, in turn, destabilizes the d-orbitals on Co with a *z*-component (*i.e.* d_{xz}, d_{yz} and d_{z^2}),

 This journal is © The Royal Society of Chemistry 2024

Published on 31 October 2024. Downloaded by Argonne Research Library on 12/20/2024 5:09:57 PM.

aligning with the calculated increase in the magnitude of D (Fig. 8). These findings demonstrate the dynamic nature of the electron distribution within the system and highlight the strong interdependence of the electron density distribution around Co with both Cl and the nearby H atoms, providing reasoning for the large effect the Cl–H interactions have on the magnetic anisotropy of the Co(II) ion in **1**.

Conclusion

In conclusion, our analysis using cantilever torque magnetometry on the distorted axially compressed octahedral complex $[CoCl_2(tu)_4]$ (**1**) revealed a tilt of the easy axis by nearly 40° relative to the Co–Cl bond. Structural investigations of **1** using synchrotron X-ray diffraction data uncovered the presence of six short Cl–H interactions, with the easy axis oriented towards the shortest of these interactions.

To understand the origin of the tilted easy axis, CASSCF-NEVPT2 calculations were performed on *in silico* modified structures of **1**. While setting equidistant Co–S bond lengths and enforcing L–Co–L angles of 90° had a modest impact on the tilt of the easy axis with respect to the Co–Cl bond, rotations around the C–N bonds to increase the Cl–H distance greatly enhanced the magnetic anisotropy of **1** by increasing the D-value by more than 25 cm^{-1} and reducing the angle between the Co–Cl bond and the easy axis by 8°.

To provide further reasoning for this result, we developed an experimental model of the electron density, derived from synchrotron data, which revealed the presence of bond critical points between the six nearby H-atoms and Cl, but no Co–H bond critical points. This provides evidence that the interactions occur through Cl rather than Co, and further investigations of the electron density show the strong polarization of Cl caused by the nearby H-atoms. Topological analysis of the calculated wavefunctions for the modified $\mathbf{1}^{ND}$ structures supported this, showing that lengthening the Cl–H distance increased the electron density in the Co–Cl bond. Consequently, this increase in electron density in the axial positions of the Co octahedra affects the energy splitting of the d-orbitals, providing a rationale for calculated increase in the magnitude of D.

Our results suggest that substituting the thiourea ligands with rigid soft donor ligands such as thiophene or ethylene thiourea holds the potential to enhance the SMM properties of **1** by preventing the H-atoms from interacting with Co through Cl. Broadening the scope, these findings demonstrate the substantial influence second coordination sphere non-covalent interactions can have on the magnetic anisotropy of transition metal complexes. While our study focuses on a specific system, it raises the question of whether similar effects might be observed in systems with stronger magnetic anisotropy or different relaxation dynamics, calling for further investigations. This research underscores the importance of exploring these interactions more comprehensively, especially considering that many methods used for studying SMMs are applied to crystals where such interactions are abundant. Furthermore, these findings open the possibility of utilizing these interactions to enhance the magnetic properties of transition metal single molecule magnets.

Author contributions

E. D. M. synthesized the single crystals of $CoCl_2(tu)_4$ for the XRD experiment, while S. S. L. synthesized the single crystals used in the CTM measurements. Y. C. collected the SC-XRD data, which were modelled by E. D. M. and S. S. L. The analysis of the obtained multipole model was performed by S. S. L. and B. B. I. The CTM data were measured, fitted, and analysed by M. P. and S. S. L. CASSCF calculations were performed by S. S. L. and analysed by S. S. L., B. B. I. and E. D. M. The manuscript was written by S. S. L. with input from all authors. M. P. and B. B. I. provided supervision and acquired funding for the study.

Data availability

Data are available from the authors upon reasonable request.

Conflicts of interest

There are no conflicts to declare.

Acknowledgements

We gratefully acknowledge the beamtime granted at ChemMatCARS at the APS. Special thanks to Lennard Krause, Mads Nielsen, and Jacob Overgaard for measuring the synchrotron data alongside Y. C. In addition, we acknowledge Jacob Overgaard for his ideas, guidance, and contributions to the multipole model analysis. Finally, we appreciate the fruitful discussions with Hannah Hedegaard Slavensky, Emil Andreasen Klahn and Vijay Parmar. The numerical results presented in this work were obtained at the Centre for Scientific Computing, Aarhus.

The study was supported by the Villum Foundation (25861), the Novo Nordisk Foundation, the Aarhus University Research Foundation and Danscatt. The financial support provided by the MUR – Dipartimenti di Eccellenza 2023–2027 (DICUS 2.0) (ref. no. B96C1700020008) to the Department of Chemistry "Ugo Schiff" of the University of Florence is acknowledged. NSF's ChemMat-CARS, Sector 15 at the Advanced Photon Source (APS), Argonne National Laboratory (ANL) is supported by the Divisions of Chemistry (CHE) and Materials Research (DMR), National Science Foundation, under grant number NSF/CHE – 1834750. This research used resources of the Advanced Photon Source, a U.S. Department of Energy (DOE) Office of Science user facility operated for the DOE Office of

Published on 31 October 2024. Downloaded by Argonne Research Library on 12/20/2024 5:09:57 PM.

Science by Argonne National Laboratory under contract no. DE-AC02-06CH11357.

References

1 A. Raza and M. Perfetti, *Coord. Chem. Rev.*, 2023, **490**, 215213.
2 M. N. Leuenberger and D. Loss, *Nature*, 2001, **410**, 789–793.
3 P. C. Stamp and A. Gaita-Arino, *J. Mater. Chem.*, 2009, **19**, 1718–1730.
4 M. Mannini, F. Pineider, P. Sainctavit, C. Danieli, E. Otero, C. Sciancalepore, A. M. Talarico, M.-A. Arrio, A. Cornia, D. Gatteschi and R. Sessoli, *Nat. Mater.*, 2009, **8**, 194–197.
5 L. Bogani and W. Wernsdorfer, *Nat. Mater.*, 2008, **7**, 179–186.
6 D. N. Woodruff, R. E. Winpenny and R. A. Layfield, *Chem. Rev.*, 2013, **113**, 5110–5148.
7 Y.-S. Meng, S.-D. Jiang, B.-W. Wang and S. Gao, *Acc. Chem. Res.*, 2016, **49**, 2381–2389.
8 K. L. Harriman and M. Murugesu, *Acc. Chem. Res.*, 2016, **49**, 1158–1167.
9 A. Castro-Alvarez, Y. Gil, L. Llanos and D. Aravena, *Inorg. Chem. Front.*, 2020, **7**, 2478–2486.
10 A. K. Bar, C. Pichon and J.-P. Sutter, *Coord. Chem. Rev.*, 2016, **308**, 346–380.
11 S. Gomez-Coca, E. Cremades, N. Aliaga-Alcalde and E. Ruiz, *J. Am. Chem. Soc.*, 2013, **135**, 7010–7018.
12 S. Gómez-Coca, D. Aravena, R. Morales and E. Ruiz, *Coord. Chem. Rev.*, 2015, **289**, 379–392.
13 P. Zhang, L. Zhang, C. Wang, S. Xue, S.-Y. Lin and J. Tang, *J. Am. Chem. Soc.*, 2014, **136**, 4484–4487.
14 A. K. Kharwar, A. Mondal and S. Konar, *Dalton Trans.*, 2021, **50**, 2832–2840.
15 N. Ishikawa, M. Sugita, T. Ishikawa, S.-Y. Koshihara and Y. Kaizu, *J. Am. Chem. Soc.*, 2003, **125**, 8694–8695.
16 K. Katoh, H. Isshiki, T. Komeda and M. Yamashita, *Coord. Chem. Rev.*, 2011, **255**, 2124–2148.
17 J. D. Rinehart and J. R. Long, *Chem. Sci.*, 2011, **2**, 2078–2085.
18 P. H. Lin, T. J. Burchell, L. Ungur, L. F. Chibotaru, W. Wernsdorfer and M. Murugesu, *Angew. Chem.*, 2009, **121**, 9653–9656.
19 J. D. Rinehart, M. Fang, W. J. Evans and J. R. Long, *J. Am. Chem. Soc.*, 2011, **133**, 14236–14239.
20 F.-S. Guo, B. M. Day, Y.-C. Chen, M.-L. Tong, A. Mansikkamäki and R. A. Layfield, *Science*, 2018, **362**, 1400–1403.
21 M. Atanasov, D. Ganyushin, D. A. Pantazis, K. Sivalingam and F. Neese, *Inorg. Chem.*, 2011, **50**, 7460–7477.
22 C. M. Legendre, E. Damgaard-Møller, J. Overgaard and D. Stalke, *Eur. J. Inorg. Chem.*, 2021, **2021**, 3108–3114.
23 E. Damgaard-Møller, L. Krause, K. Tolborg, G. Macetti, A. Genoni and J. Overgaard, *Angew. Chem.*, 2020, **132**, 21389–21395.
24 S. Gómez-Coca, A. Urtizberea, E. Cremades, P. J. Alonso, A. Camón, E. Ruiz and F. Luis, *Nat. Commun.*, 2014, **5**, 4300.
25 R. Mitsuhashi, S. Hosoya, T. Suzuki, Y. Sunatsuki, H. Sakiyama and M. Mikuriya, *RSC Adv.*, 2020, **10**, 43472–43479.
26 P. C. Bunting, M. Atanasov, E. Damgaard-Møller, M. Perfetti, I. Crassee, M. Orlita, J. Overgaard, J. van Slageren, F. Neese and J. R. Long, *Science*, 2018, **362**, eaat7319.
27 B. Matheson, T. N. Dais, M. Donaldson, G. J. Rowlands and P. Plieger, *Inorg. Chem. Front.*, 2023, **10**, 6427–6439.
28 R. Herchel, P. Zoufalý and I. Nemec, *RSC Adv.*, 2019, **9**, 569–575.
29 Y. Gil, L. Llanos, P. Cancino, P. Fuentealba, A. Vega, E. Spodine and D. Aravena, *J. Phys. Chem. C*, 2020, **124**, 5308–5320.
30 A. B. Canaj, M. K. Singh, C. Wilson, G. Rajaraman and M. Murrie, *Chem. Commun.*, 2018, **54**, 8273–8276.
31 S. K. Gupta, S. Dey, T. Rajeshkumar, G. Rajaraman and R. Murugavel, *Chem. – Eur. J.*, 2022, **28**, e202103585.
32 O. Kahn, *Molecular magnetism*, Courier Dover Publications, 2021.
33 S. Tripathi, S. Vaidya, N. Ahmed, E. Andreasen Klahn, H. Cao, L. Spillecke, C. Koo, S. Spachmann, R. Klingeler, G. Rajaraman, J. Overgaard and M. Shanmugam, *Cell Rep. Phys. Sci.*, 2021, **2**, 100404.
34 K. Ridier, B. Gillon, A. Gukasov, G. Chaboussant, A. Cousson, D. Luneau, A. Borta, J.-F. Jacquot, R. Checa, Y. Chiba, H. Sakiyama and M. Mikuriya, *Chem. – Eur. J.*, 2016, **22**, 724–735.
35 F. Neese, *Wiley Interdiscip. Rev.: Comput. Mol. Sci.*, 2018, **8**, e1327.
36 L. Krause, *pilatus3-fc*, 2019.
37 *SAINT Integration Engine (8.38A)*, Bruker AXS Inc., Madison, WI, USA, 2013.
38 L. Krause, R. Herbst-Irmer, G. M. Sheldrick and D. Stalke, *J. Appl. Crystallogr.*, 2015, **48**, 3–10.
39 R. Blessing, *J. Appl. Crystallogr.*, 1997, **30**, 421–426.
40 C. B. Hubschle, G. M. Sheldrick and B. Dittrich, *J. Appl. Crystallogr.*, 2011, **44**, 1281–1284.
41 P. M. A. Volkov, L. J. Farrugia, C. Gatti, P. Mallinson, T. Richter and T. Koritsanszky, *XD2016 - A Computer Program Package for Multipole Renement, Topological Analysis of Charge Densities and Evaluation of Intermolecular Energies from Experimental and Theoretical Structure Factors*, 2016.
42 N. K. Hansen and P. Coppens, *Acta Crystallogr., Sect. A: Cryst. Phys., Diffr., Theor. Gen. Crystallogr.*, 1978, **34**, 909–921.
43 E. Damgaard-Møller, L. Krause and J. Overgaard, in *21st Century Challenges in Chemical Crystallography II: Structural Correlations and Data Interpretation*, ed. D. Michael, P. Mingos and P. R. Raithby, Springer International Publishing, Cham, 2020, pp. 145–182, DOI: **10.1007/430_2020_61**.
44 F. H. Allen and I. J. Bruno, *Acta Crystallogr., Sect. B: Struct. Sci.*, 2010, **66**, 380–386.
45 A. Volkov and P. Coppens, *Acta Crystallogr., Sect. A: Found. Crystallogr.*, 2001, **57**, 395–405.
46 M. Douglas and N. M. Kroll, *Ann. Phys.*, 1974, **82**, 89–155.

 This journal is © The Royal Society of Chemistry 2024

47 B. A. Hess, *Phys. Rev. A*, 1985, **32**, 756.
48 D. Ganyushin and F. Neese, *J. Chem. Phys.*, 2013, **138**, 104113.
49 M. Atanasov, D. Aravena, E. Suturina, E. Bill, D. Maganas and F. Neese, *Coord. Chem. Rev.*, 2015, **289**, 177–214.
50 D. Ganyushin and F. Neese, *J. Chem. Phys.*, 2006, **125**, 24103.
51 F. Neese, *J. Chem. Phys.*, 2005, **122**, 34107.
52 M. Perfetti, *Coord. Chem. Rev.*, 2017, **348**, 171–186.
53 *MATLAB*, The MathWorks, Inc., 2022.
54 S. Stoll and A. Schweiger, *J. Magn. Reson.*, 2006, **178**, 42–55.
55 D. Stalke, *Chem. – Eur. J.*, 2011, **17**, 9264–9278.
56 T. A. Keith, *AIMAll (19.10.12)*, TK Gristmill Software, Overland Park KS, USA, 2019.

Published on 31 October 2024. Downloaded by Argonne Research Library on 12/20/2024 5:09:57 PM.